



Excess conductivity and magnetoresistance analysis for (BSF)_x/(Bi, Pb)-2223 composite

M. Matar¹ · I. E. Mohamed^{1,2} · A. I. Abou-Aly¹ · R. Awad¹ · M. Anas¹ · M. S. Hassan¹

Received: 9 November 2023 / Accepted: 12 February 2024
© The Author(s) 2024

Abstract

This study examined the impact of adding hard ferrite Ba_{0.5}Sr_{0.5}Fe₁₂O₁₉ (BSF) nanoparticles to the Bi_{1.8}Pb_{0.4}Sr₂Ca₂Cu_{3.2}O_{10+δ} (Bi, Pb)-2223 superconductor phase. The investigation specifically focused on evaluating the critical current density, fluctuation-induced conductivity, and magnetoresistance of nano-(BSF)_x/(Bi, Pb)-2223 composite, where 0.00 ≤ *x* ≤ 0.20 wt.%. The results revealed that the critical current density, *J_c*, increased with the addition of nano-(BSF) up to *x* = 0.04 wt.%, reaching a value of 441.20 A/cm². The Aslamazov and Larkin (A–L) approach has been evaluated the fluctuation-induced conductivity. Several superconducting parameters, including coherence length $\zeta_c(0)$, effective layer thickness *d*, penetration depth $\lambda_{pd}(0)$, and Fermi energy *E_F* showed improvement as the concentration of nano-(BSF) increased up to *x* = 0.04 wt.%. In addition to Ginzburg–Landau critical parameters, such as the thermodynamic critical field *B_c(0)*, lower critical magnetic field *B_{c1}(0)*, upper critical magnetic field *B_{c2}(0)*, and critical current density *J_c(0)* demonstrated an increase up to *x* = 0.04 wt.%, followed by a decrease for higher concentrations. The magnetoresistance measurements were performed at various applied DC magnetic fields, with values ranging from 0.29 to 4.44 kG, and were analyzed using the thermally activated flux creep (TAFC) and Ambegaokar–Halperin (AH) models. The calculated flux pinning energy (*U*) increased with the addition of nano-(BSF) up to *x* = 0.04 wt.% and then decreased for *x* > 0.04 wt.%. Furthermore, the transition width (ΔT), was observed to increase as the applied magnetic field values increased. Moreover, the addition of nano-(BSF) increased the field-independent critical current density, *J_{c0}(0)*, up to *x* = 0.04 wt.%, after which it decreased for higher concentrations.

Keywords Nano-(BSF)_x/(Bi, Pb)-2223 · Critical current density · Excess conductivity · Magnetoresistance · Flux pinning energy

1 Introduction

The (Bi, Pb)-2223 superconductor phase has garnered significant attention due to its higher superconducting transition temperature, critical current density, and magnetic field carrying capacity. These characteristics have made it a promising material for numerous technological and industrial applications [1]. However, the application of the (Bi, Pb)-2223 phase is limited by several disadvantages, particularly in high magnetic fields and temperatures. These limitations stem from weak links, high anisotropy, and a short

coherence length, as well as a long penetration depth [2, 3]. Therefore, researchers have endeavored to enhance the electrical characteristics of the (Bi, Pb)-2223 superconducting phase through various methods and techniques. The introduction of nanoparticle materials has been widely used and has effectively enhanced the flux pinning strength by creating artificial pinning centers beside those formed naturally in the superconducting phase, leading to improvement in the (Bi, Pb)-2223 superconducting properties [4–13].

Excess conductivity investigations have garnered significant attention in high-temperature superconducting (HTSC) materials, particularly the (Bi, Pb)-2223 phase, to better understand and clarify their intrinsic superconducting properties [7, 14, 15]. Aftabi et al. [16] studied the effect of adding ZnO nanoparticles to investigate the fluctuation-induced conductivity of the (Bi, Pb)-2223 phase. They found that the addition of 0.20 wt.% ZnO nanoparticles improved the superconducting parameters of the (Bi, Pb)-2223 phase.

✉ M. S. Hassan
mohammedscience2013@alexu.edu.eg

¹ Department of Physics, Faculty of Science, Alexandria University, Alexandria, Egypt

² Department of Physics, Faculty of Education, West Kordofan University, Al-Nuhud, Sudan

Additionally, Awad et al. [17] reported that the addition of NiO nanoparticles enhanced the excess conductivity parameters such as $\xi_c(0)$, d and J of (Bi, Pb)-2223 phase.

On the other hand, the broadening of the resistivity transition in the (Bi, Pb)-2223 superconducting phase under an applied magnetic field has garnered significant interest. Several researchers have provided valuable insights to enhance the pinning properties. [18–22]. Zouaoui et al. [23] added ZrO₂ nanosized particles to the (Bi, Pb)-2223 phase to investigate the flux pinning properties. They found that the addition of 0.10 wt.% of ZrO₂ nanoparticles improved the superconducting properties in an applied magnetic field. Barakat et al. [24] improved the magnetic properties of the (Bi, Pb)-2223 superconducting phase by adding up to 0.50 wt.% of BaSnO₃ nanoparticles.

To the best of the authors' knowledge, the current study presents the first analysis of the impact of Ba_{0.5}Sr_{0.5}Fe₁₂O₁₉ (BSF) nanoparticles on the fluctuation-induced conductivity and on the measured resistive transitions of (Bi, Pb)-2223 superconducting phase at different applied magnetic fields. For this purpose, nano-(BSF)_x/(Bi, Pb)-2223 composites with $0.00 \leq x \leq 0.20$ wt.% were synthesized through the solid-state method. To comprehend the role of BSF nanoparticles addition in the (Bi, Pb)-2223 matrix, the electrical resistivity data were analyzed with the aid of Aslamazov–Larkin (A–L) model. The fluctuation-induced conductivity of the prepared composites was studied. Numerous fundamental superconducting parameters, such as coherence length along c-axis $\xi_c(0)$, effective layer thickness d , penetration depth $\lambda_{pd}(0)$, Fermi energy E_F , thermodynamic critical field $B_c(0)$, lower critical magnetic field $B_{c1}(0)$, upper critical magnetic field $B_{c2}(0)$, and critical current density $J_c(0)$, were estimated as function of BSF content. Finally, the magnetoresistance of nano-(BSF)_x/(Bi, Pb)-2223 composites was studied under different applied fields in the range of 0.29–4.44 kG. The superconducting parameters, such as flux pinning energy, $U(B)$ and $J_c(0)$ were calculated based on thermally activated flux creep (T AFC) and Ambegaokar–Halperin (AH) models for HTSC materials.

2 Experimental procedure

In our previous work, we thoroughly described the preparation procedure of nano-(BSF)_x/(Bi, Pb)-2223 composite samples, with $x = 0.00, 0.01, 0.02, 0.03, 0.04, 0.05, 0.10,$ and 0.20 wt.%, as outlined by Hassan et al. [4]. In this study, the same samples underwent analysis using energy dispersive X-rays (EDX) via a JEOL device (model JSM-IT200) to determine the elemental composition and distribution of nanoparticles in the composite samples. Additionally, X-ray photoelectron spectroscopy (XPS) was utilized, employing a

KRATOS X SAM 800 spectrometer, to examine the elemental composition and oxidation states of the elements.

The critical current density as a function of voltage (I–V) was measured at 77 K using the four-probe method [25]. The fluctuation-induced excess conductivity analysis for the composite samples was investigated from resistivity data. The temperature dependence of the resistivity was measured under various magnetic fields, with values ranging from 0.29 to 4.44 kG, generated by a DC electromagnet. The samples were cooled until the temperature reached its zero-resistivity temperature (T_0) using helium gas through a cryogenic diplex system. Then the measurements were carried out in a magnetic field applied perpendicular to the direction of the driving current of 1 mA, upon heating after zero-field cooling (ZFC).

3 Results and discussion

3.1 Nano-(BSF) characterization

The nano-(BSF) particles were previously characterized and analyzed by Yassine et al. [26]. Transmission electron microscopy (TEM) revealed an average particle size of 48.987 nm, falling within the range of the coherence length (ξ) and penetration depth (λ) of the (Bi, Pb)-2223 phase. To enhance the flux pinning mechanism in the (Bi, Pb)-2223 phase, the nanoparticle size should be greater than (ξ) yet less than (λ) [13, 27]. Additionally, these nanoparticles possess hard magnetic ferrite characteristics with coercive field ($H_c = 5819.6$ G), saturation magnetization ($M_s = 56.644$ emu/g) and remanent magnetization ($M_r = 27.968$ emu/g).

3.2 Nano-(BSF)_x/(Bi, Pb)-2223 composite samples characterization

Hassan et al. [4], previously conducted a structural analysis of the composite samples using X-ray diffraction (XRD) and scanning electron microscopy (SEM), with results summarized in Table 1. Among these samples, the nano-(BSF)_x/(Bi, Pb)-2223 composite with $x = 0.04$ wt.% exhibits a higher volume fraction of the main phase, lower volume fractions of (Bi, Pb)-2212 and Ca₂PbO₄ impurity phases, and the best grain growth, featuring an average grain size of 2.940 μm .

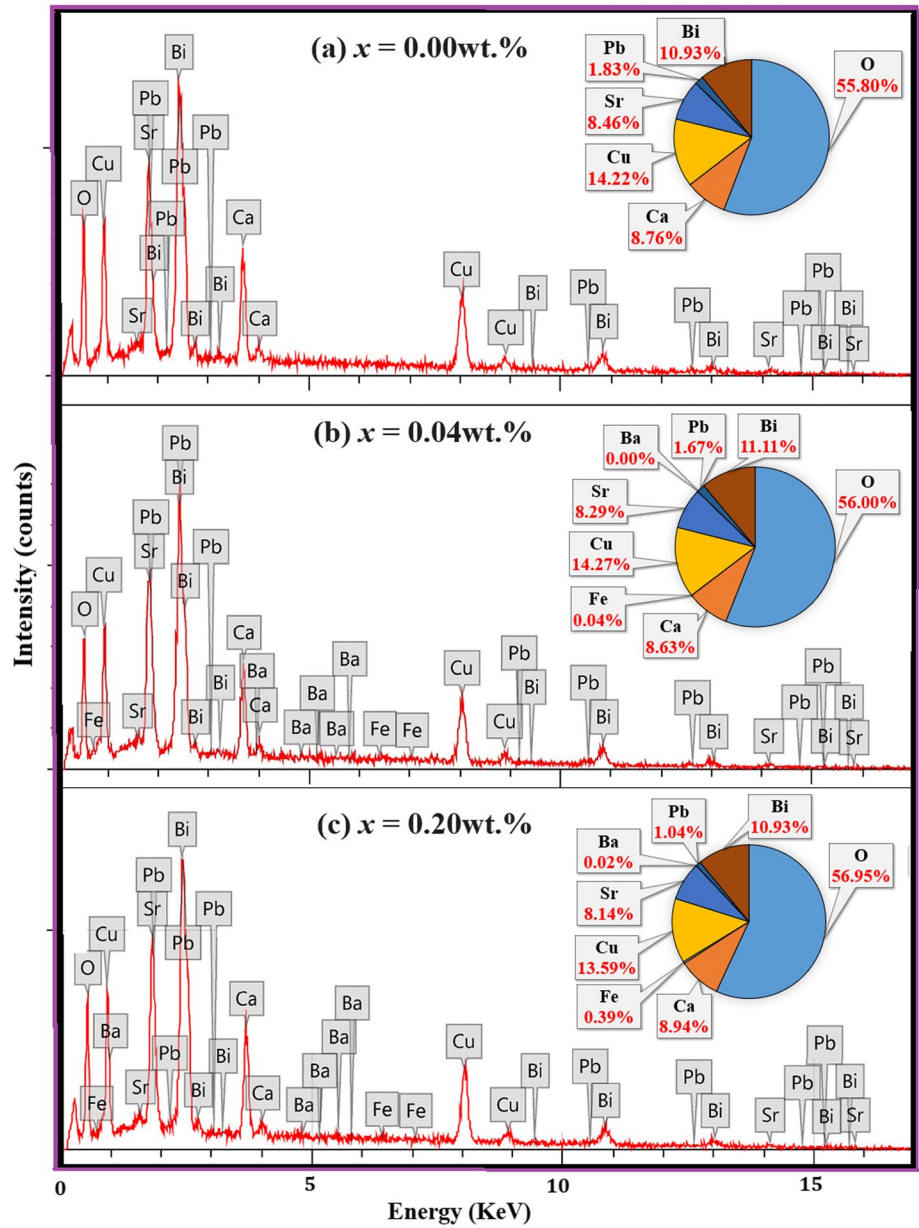
3.2.1 EDX analysis

EDX analysis was employed to determine the chemical composition and clarify the homogeneity of the prepared samples. Figure 1 illustrates the EDX spectra of composite samples nano-(BSF)_x/(Bi, Pb)-2223, with $x = 0.00, 0.04,$ and 0.20 wt.%, respectively.

Table 1 XRD and SEM parameters of nano-(BSF)_x/(Bi, Pb)-2223 composite samples with 0.00 ≤ *x* ≤ 0.20

<i>x</i> (wt.%)		0.00	0.01	0.02	0.03	0.04	0.05	0.10	0.20
Volume fraction %	Bi-2223	80.277	80.521	81.344	84.446	87.865	83.486	79.792	76.992
	Bi-2212	17.151	16.674	15.987	13.114	10.537	13.7	17.135	19.957
	Ca ₂ PbO ₄	2.572	2.805	2.669	2.44	1.598	2.814	3.073	3.051
Lattice Parameter (Å)	<i>a</i>	5.401	5.406	5.413	5.417	5.406	5.409	5.402	5.418
	<i>b</i>	5.443	5.46	5.447	5.436	5.46	5.428	5.439	5.443
	<i>c</i>	37.191	37.585	37.513	37.214	37.025	37.425	37.095	37.507
Average grain size (μm)		1.630	1.858	1.936	2.563	2.940	2.365	1.175	1.089
Porosity %		30.139	29.190	27.710	25.718	24.409	25.467	34.188	36.317

Fig. 1 EDX spectra of nano-(BSF)_x/(Bi, Pb)-2223 composite samples with *x* = 0.00, 0.04, and 0.20 wt.%



It is worth mentioning that no undesirable elements were detected. Furthermore, the peak positions of the elements

Bi, Pb, Sr, Ca, and Cu remained unchanged following the addition of nano-(BSF). Additionally, the added samples

exhibited peaks corresponding to Ba and Fe elements. The EDX analysis revealed that nano-(BSF) does not integrate into the structure of the (Bi, Pb)-2223 phase; rather, they exist interstitially between the grain boundaries. This result is confirmed by the XRD data, which showed that there is no significant difference in lattice parameter values as shown in Table 1, indicating the absence of undesirable elements in the samples and confirming that there was no contamination during the synthesis process. Similar findings regarding nanoparticle addition, where the nanoparticles are located interstitially between the grains and do not enter the structure of the (Bi, Pb)-2223 phase, were reported by Oboudi [28] when he added Y_2O_3 nanoparticles and El Makdah et al. [29] when they added YIG nanoparticles. In addition the SEM analysis results in our previous study [4] also confirm these findings. Moreover, as x increases, the composite samples exhibit an increase in the weight percentage of Ba, Fe, and O originating from the nanoparticles. The inset graphs

in Fig. 1 summarize the atomic percentages of the compositional components.

It is noticed that the spectra for the three regions, as shown in Fig. 2, are almost identical which indicates the high homogeneity of the prepared samples. This homogeneity can be ascribed to the addition of nano-(BSF) during the latter stages of the superconductor preparation process when the (Bi, Pb)-2223 superconducting phase is nearly fully formed. This interpretation aligns with earlier reports when SmIG [5] and YIG [29] nanoparticles were added to the (Bi, Pb)-2223 phase.

3.2.2 XPS analysis

The analysis conducted using XPS for the nano-(BSF)_x/(Bi, Pb)-2223 composite samples aimed to corroborate the previously obtained XRD data analysis results and determine the

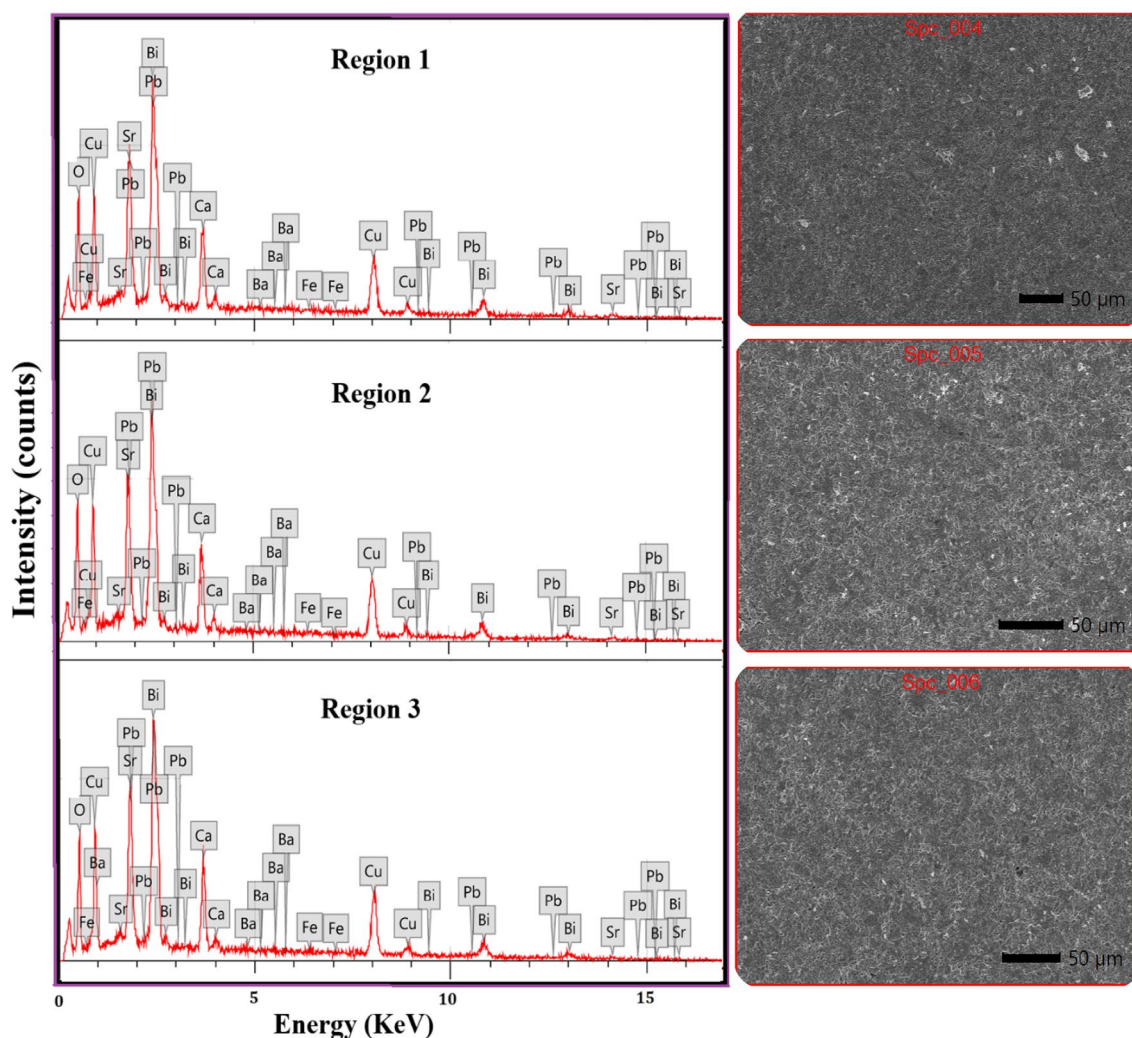


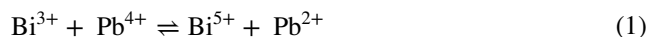
Fig. 2 Three spectral shots from three distinct areas of the nano-(BSF)_x/(Bi, Pb)-2223 composite sample with $x=0.20$ wt.%

binding energies and oxidation states of different elements within the composite samples.

Figure 3 shows the XPS spectra survey scan for nano-(BSF)_x/(Bi, Pb)-2223 composite of the pure, 0.04, and 0.20 wt.% samples, the scanning range extended from 0 to 1000 eV. The survey spectra for all the samples revealed the presence of bismuth (Bi), lead (Pb), strontium (Sr), calcium (Ca), copper (Cu), oxygen (O), and small traces of carbon (C). The appearance of C in the spectra of all samples is attributed to the sample's interaction with CO₂ in ambient air before XPS measurement [29–32]. Furthermore, the survey spectra for the composite samples with $x=0.04$ and 0.20 wt.% reveal, in addition to the elements mentioned above, the presence of Ba 3d with a binding energy of around 780 eV, related to the Ba 3d_{3/2} state [33, 34]. As well as Fe 2p with a binding energy of around 711 and 719 eV, related to the Fe 2p_{3/2} and Fe 2p_{1/2} states [35] originating from the addition of nanoparticles. The intensity of Sr in the nano is very small and cannot be seen because it overlaps with the high-intensity Sr peak of the superconductor. The result of Ba, Sr and Fe elements matches the XPS analysis of the nanoparticles obtained earlier by Yassine et al. [26]. Moreover, the high-resolution XPS spectra of the elements Bi, Sr, Ca, Pb and Cu of the composite samples were deconvoluted in Fig. 4 to study the major peaks of each component. In addition, Table 2 represents the values of the binding energy (BE) and full width at half maximum (FWHM) of each element.

The spectra of the core states of Bi 4f consist of two peaks, corresponding to Bi 4f_{5/2} and Bi 4f_{7/2}, as shown in Fig. 4a. The position of Bi 4f_{5/2} binding energy lines for all samples is identical to that in the case of the Bi₂O₃ [36], which corresponds to the Bi³⁺ oxidation state. The absence of a higher binding energy (HBE) peak corresponding to

Bi⁵⁺ valency states suggests that the Bi 4f spectrum is close to being in a single chemical state. Furthermore, the binding energy positions of the component Bi 4f_{7/2} as it slightly deviates from 159.08 eV for the pure sample to 158.1 eV for the sample with $x=0.20$ wt.%, with the existence of a decrease in FWHM. This can be attributed to the fact that a portion of Bi³⁺ was oxidized by the Pb⁴⁺ ions to form Bi⁵⁺, according to the following reaction (1) [31].



On the other hand, the addition of nano-(BSF) may have contributed to an increase in oxygen content near the Bi–O layers, leading to slight deviations from Bi³⁺, as found above in the EDX analysis. Consequently, the heightened valency of Bi leads to increased Coulomb attraction within the Bi–O layers. Additionally, the insulating Bi–O layers hinder the maintenance of superconducting phase coherence between the CuO₂ planes [37, 38]. This confirms our previously obtained results of T_c at higher concentrations.

The Sr 3d peak was observed to consist of two peaks, ascribed to different chemical states, namely Sr 3d_{3/2} and Sr 3d_{5/2}, as shown in Fig. 4b. The energy separation between each coordination state is 1.2 eV for the pure sample, 1.16 eV for $x=0.04$ wt.%, and 1.52 eV for $x=0.20$ wt.%. It was noted that the binding energy of each component shifted with the addition of nanoparticles, accompanied by an increase in FWHM. This change is particularly noticeable for the Sr 4f_{5/2} component, increasing the peak area, especially for the sample with $x=0.20$ wt.%. The shift in the binding energy could be attributed to the higher coordination state sites between the two Cu–O planes, which are more likely to be occupied by Sr than the lower coordination state sites between the Bi–O and the adjacent Cu–O planes with the addition of nano-(BSF). Similar findings were reported by Koichi. [31] when he studied the (Bi, Pb)-2223 phase by substituting of BiF₃ for Bi₂O₃. The increase in the peak of the Sr 4f_{5/2} component may be attributed to the presence of strontium in the nanoparticles.

The deconvoluted spectra of Ca 2p and Pb 4f were observed, each consisting of two components, as shown in Fig. 4c, d. No significant difference was observed in binding energy and FWHM for Ca 2p and Pb 4f components in all samples as seen in Table 2. The presence of lead (Pb) in two separate oxidation states within the Pb 4f spectra can be attributed to different chemical states of lead with distinct valences, as shown in the equilibrium reaction (2) [37]. Specifically, Pb²⁺ integrates into the lattice of the (Bi, Pb)-2223 phase, occupying the Bi positions within the double Bi–O layers. On the other hand, Pb⁴⁺ is found within the Ca₂PbO₄ compound [29, 30, 37]. This explanation aligns perfectly

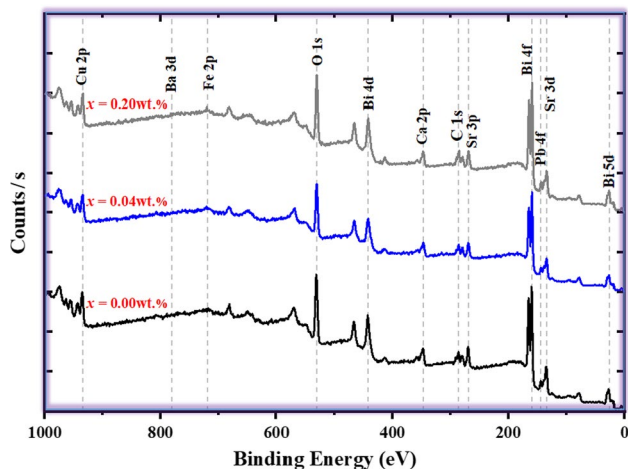


Fig. 3 XPS survey scan of nano-(BSF)_x/(Bi, Pb)-2223 composite samples with $x=0.00$, 0.04, and 0.20 wt.%

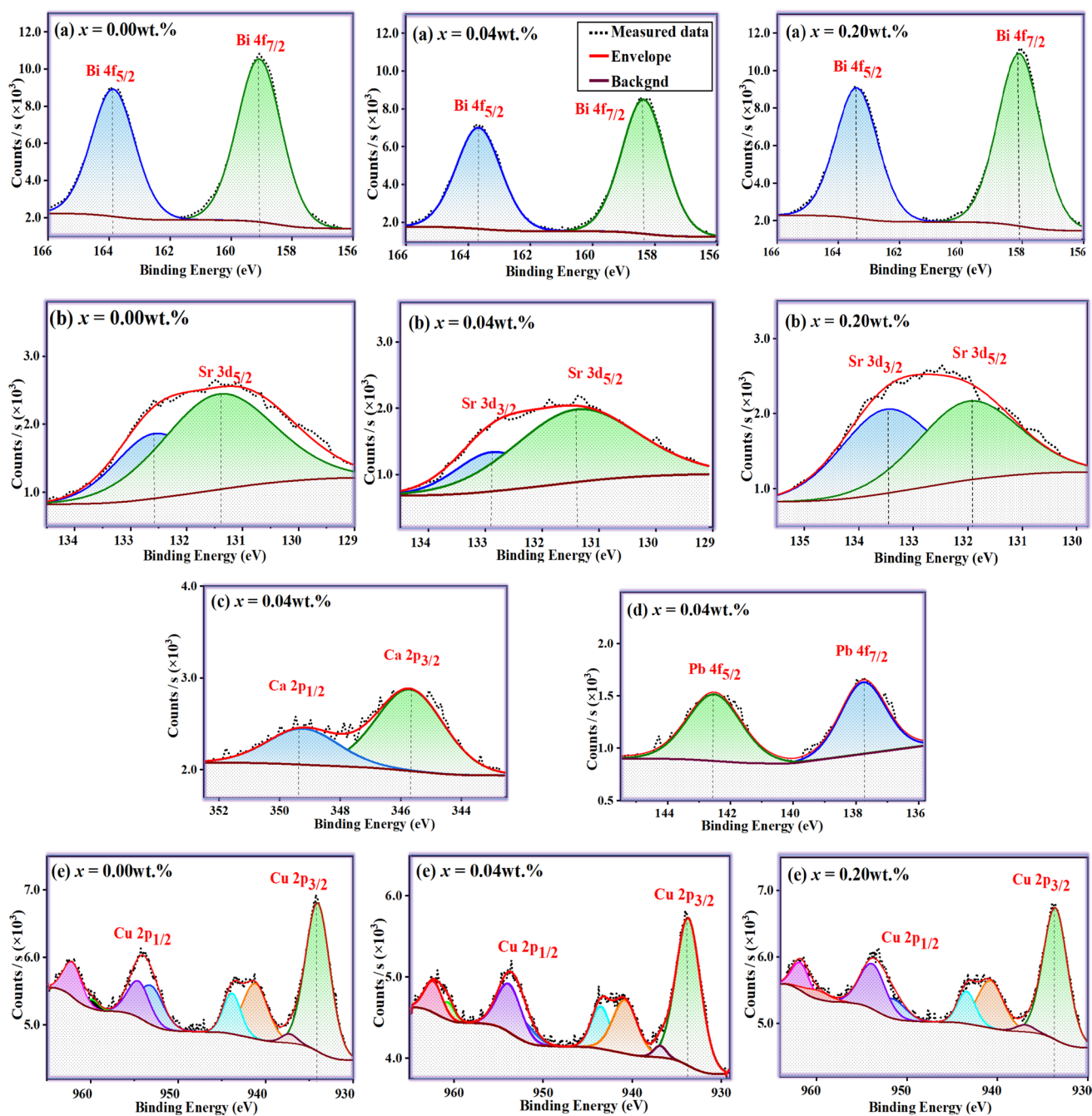


Fig. 4 The deconvolution spectra of **a** Bi 4f, **b** Sr 3d, **c** Ca 2p, **d** Pb 4f and **e** Cu-2p of the nano-(BSF)_x/(Bi, Pb)-2223 composite samples with $x = 0.00, 0.04$ and 0.20 wt. %

with the findings from structure investigations by the XRD analysis in our previous study [4].

The deconvoluted Cu 2p spectra are displayed in Fig. 4e. As shown the spectra exhibit spin-orbit split main lines Cu 2p_{3/2} and Cu 2p_{1/2}, along with their respective satellites, which are observed at approximately 9 eV from each main line in all samples. This is recognized as a characteristic feature of Cu 2p XPS high-resolution spectra. The primary

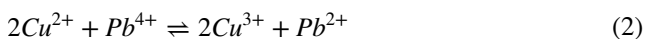
spectral lines and their associated satellites correspond to the d⁹ and d¹⁰ final states, as documented in the existing literature [30, 31, 38]. The Cu 2p_{3/2} line signified the existence of Cu³⁺ valency, particularly in the high binding energy component. This valency is essential for charge neutrality and the formation of the (Bi, Pb)-2223 superconductor. This observation is attributed to the oxidation of Cu²⁺ to Cu³⁺, increasing hole carrier concentrations and, consequently,

Table 2 The binding energies (BE) (± 0.1 eV) and full width at half maximum (FWHM) (± 0.01 eV) of composite elements

	Elements	x (wt.%)									
		Bi		Sr		Cu		Ca		Pb	
		Bi 4f 7/2	Bi 4f 5/2	Sr 3d 5/2	Sr 3d 3/2	Cu 2p 3/2	Cu 2p 1/2	Ca 2p 3/2	Ca 2p 1/2	Pb 4f 7/2	Pb 4f 5/2
0.00	BE (eV)	159.08	163.88	131.37	132.58	934.06	953.13	345.68	349.54	137.89	142.69
	FWHM (eV)	1.71	1.68	2.30	1.66	3.31	3.37	2.76	2.95	1.58	1.84
0.04	BE (eV)	158.37	163.67	131.74	132.9	933.74	952.42	345.70	349.23	137.77	142.52
	FWHM (eV)	1.70	1.66	2.56	1.19	3.25	3.37	2.78	2.65	1.71	2.01
0.20	BE (eV)	158.10	163.41	131.95	133.47	933.61	953.38	345.78	349.56	137.45	142.23
	FWHM (eV)	1.66	1.62	2.20	1.99	3.19	3.37	2.80	2.45	1.49	1.76

an enhancement in the conductivity of the (Bi, Pb)-2223 phase. Comparable results were reported by. El Makdah et al. [29] in their study when they added YIG nanoparticles and Sekhar et al. [36] in their X-ray photoelectron spectroscopy study of Bi₂Sr₂Ca_{1-x}Eu_xCu₂O_y.

Considering what has come before, the cationic equilibrium mechanism described in reaction (2) determines the valency of the Pb ions.



3.3 Electrical transport properties

3.3.1 Electrical resistivity measurements

The electrical resistivity for nano-(BSF)_x/(Bi, Pb)-2223 composite samples were measured and discussed previously by Hassan et al. [4]. Table 3 presents a summary of the electrical resistivity parameters. As shown, the sample with $x=0.04$ wt.% exhibited enhancements in transition temperature (T_c), zero-resistivity temperature (T_0), transition width (ΔT), as well as other resistivity parameters such as normal state resistivity (ρ_n), residual resistivity (ρ_0), and resistivity temperature coefficient (α). This enhancement was attributed to improvements in the volume fraction and inter-grain connectivity, as indicated in Table 1.

Table 3 Electrical resistivity parameters of nano-(BSF)_x/(Bi, Pb)-2223 composite samples with $0.00 \leq x \leq 0.20$

x (wt.%)	0.00	0.01	0.02	0.03	0.04	0.05	0.10	0.20
T_c (K)	107.831	108.487	109.647	110.909	112.44	107.57	100.699	86.024
T_0 (K)	93.250	96.000	98.500	101.000	103.500	98.500	87.700	71.000
ΔT (K)	14.581	12.487	11.147	9.909	8.940	9.070	12.999	15.024
ρ_n (m Ω cm)	2.060	1.989	1.881	1.618	1.170	1.448	2.242	2.360
ρ_0 (m Ω cm)	0.528	0.955	0.565	0.515	0.4587	0.575	0.788	0.991
$\alpha \times 10^{-3}$ (m Ω cm K ⁻¹)	5.227	3.947	4.461	3.630	2.314	2.918	4.538	4.577
P	0.138	0.139	0.143	0.147	0.160	0.137	0.124	0.107
S (μ V/K)	38.608	37.421	35.081	31.949	23.433	39.061	48.662	63.676

The hole-carrier concentrations (P) within the CuO₂ planes, which can impact the superconducting characteristics of the (Bi, Pb)-2223 superconducting phase, including the critical temperature, were calculated from the electrical resistivity values using the following relation [24, 39] and tabulated in Table 3:

$$P = 0.16 - \left[\frac{\left(1 - \frac{T_c}{T_{cmax}}\right)}{82.6} \right]^{0.5}, \tag{3}$$

where T_{cmax} is taken as 110 K for the (Bi, Pb)-2223 phase [40]. As demonstrated in Table 3 the values of P vary between 0.107 to 0.160 which is consistency with the theoretical studies which indicated that the hole concentration value for (Bi, Pb)-2223 phase falls within the range of 0.116 to 0.160 [41, 42]. The P values increase from 0.138 for the pure sample to 0.160 for $x=0.04$ wt.% and then decrease to 0.107 for the sample with $x=0.20$ wt.%. This suggests that the addition of nano-(BSF), up to $x=0.04$ wt.%, has a positive effect on the hole-carrier concentrations. This confirms the results of the improvement in T_c that we obtained in our previous study [4]. Thus, this improvement contributes to optimizing the superconducting properties of the (Bi, Pb)-2223 phase. On the contrary, an increase in nano-(BSF) beyond 0.04 wt.% affects the hole concentration and reduces

the carrier density, thereby diminishing the superconducting properties of the (Bi, Pb)-2223 phase.

Furthermore, the charge carrier transport mechanism in HTSC is determined by the thermoelectric power (S) [43, 44]. These are calculated based on the values of P , as described by Eq. (4), and are listed in Table 3.

$$S = \frac{K_B}{e} \left[\ln \left(\frac{1-P}{2P} \right) - \ln 2 \right], \quad (4)$$

where k_B is the Boltzmann constant, e is the electron charge and P is the hole-carrier concentration. It is noticed that in Table 3, the thermoelectric power values of the composite samples are all positive, suggesting that hole conduction in CuO_2 planes is the predominant mechanism by holes (p-type behavior) [44, 45]. Additionally, the values of S decreased as x increased up to $x=0.04$ wt.%, aligning with the change in hole concentration that increased in electronic carriers per Cu atom in the CuO_2 layer. On the contrary, S increased for $x > 0.04$ wt.%, which could be attributed to the growth of impurities and an inhomogeneous distribution with higher concentrations of nanoparticles.

3.3.2 Critical current density (J_c) measurements

The J_c of the HTSC materials is an important factor for its practical applications, in particular (Bi, Pb)-2223 superconductor phase due to its high T_c . When an external current is applied to the (Bi, Pb)-2223 superconducting phase in the mixed state, it exerts a force on the vortices, causing the flux lines to move once this current reaches a critical threshold value. The motion of vortices dissipates energy, and as a result, the superconductor loses its current-carrying ability, which significantly affects its superconducting performance

[46–48]. Therefore, in this study, the addition of hard ferrite nanoparticles on the (Bi, Pb)-2223 superconducting phase is expected to pin the vortices or immobilize their motion, thereby enhancing the current-carrying capacity.

The J_c of nano-(BSF) $_x$ /(Bi, Pb)-2223 composite samples were measured by applying a direct current to the superconductor while measuring the voltage across it at a fixed temperature of 77 K. The E - J curves are obtained and presented in Fig. 5a and the J_c values are determined using Ekin's offset method [49], by taking a tangent line to the E - J curve at a specific electric field level and extending it to where the electric field becomes zero. Then the J_c values are illustrated in Fig. 5b as a function of doping x (wt.%).

As seen in Fig. 5a nano-(BSF) $_x$ /(Bi, Pb)-2223 composite samples exhibited the same behavior. In the thermal Activation flux flow (TAFF) region, E - J is a bit linear, where $J \ll J_c$, which means that a vortex flows due to dissipation is promoted by thermal excitations [50]. In the flux creep a voltage drop appears showing an exponential behavior at a certain value of applied current $J \approx J_c$. This signifies the generation of vortices motion, which in turn scatter the charge carriers. The flow in this region resembles turbulent flow, leading to an increase in sample resistance due to the weak link junctions that impede the motion of flux [50, 51]. In the flux flow region, the abrupt increase in E the $J \gg J_c$, where the pinning force is much weaker than the driving force. Consequently, diffusive vortex motion occurs. Therefore, forming eddy currents that generate a magnetic field. This magnetic field disrupts the superconductivity, causing the sample to behave like a normal conductor [52, 53].

It's noteworthy that the calculated critical current density values increased from 151.090 A/cm^2 for the pure sample to 441.200 A/cm^2 for the sample with $x=0.04$ wt.%. This represents a significant enhancement of the

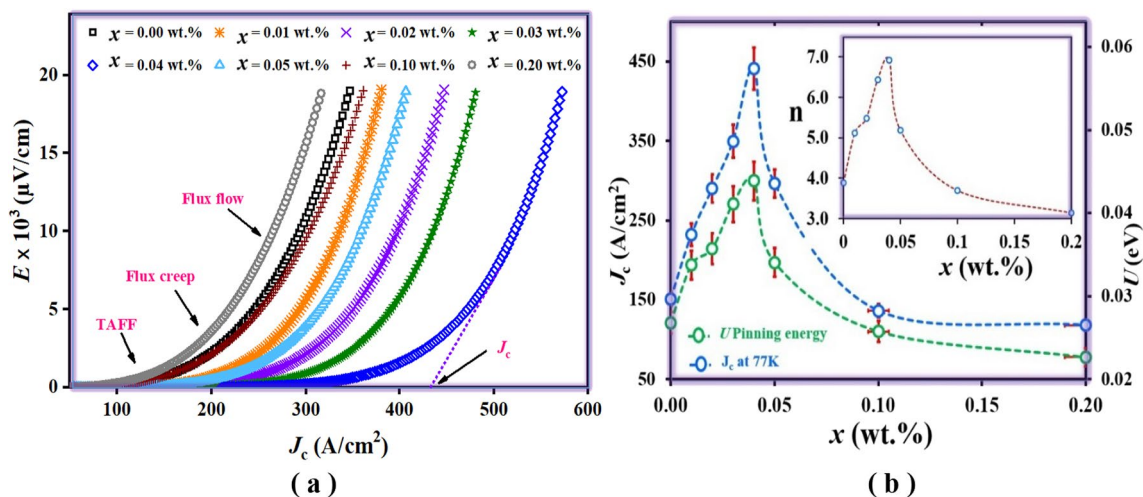


Fig. 5 **a** E - J curves and **b** variation of J_c and U for nano-(BSF) $_x$ /(Bi, Pb)-2223 composite samples with $0.00 \leq x \leq 0.20$

J_c . This improvement can be attributed to the addition of hard ferrite nano-(BSF), which enhances vortex pinning strength by acting as pinning centers. These nanoparticles efficiently immobilize vortices and facilitate inter-grain connections and intergranular flux pinning, leading to an increase in the J_c . These findings are consistent with the enhancement in the volume fraction of the (Bi, Pb)-2223 phase, and grain's conductivity by increasing the average grain size and decreasing the porosity % that was obtained by SEM analysis results, as was in Table 1. This indicated an enhancement in intergranular coupling and a reduction in the number of weak links. A similar result was observed by El Makdah et al. [29] when they added YIG nanoparticles, and Habanjar et al. [6] they added BaFe₁₂O₁₉ nanoparticles, on the (Bi,Pb)-2223 phase. On the contrary, with a further increase in nano-(BSF) $x > 0.04$ wt.%, the J_c decreases. This decrease could be attributed to the significant aggregation of nano-(BSF) between the grains, rather than at the grain boundaries, leading to a reduction in inter-grain connectivity, and the formation of (Bi, Pb)-2212 increases. This, in turn, results in a decrease in the J_c .

On the other hand, the E - J curve can be described by the power-law relation provided in Eq. (5):

$$E = \beta J^n. \quad (5)$$

Here, β and n represent experimental or material constants. The exponent value n serves as an additional parameter describing the homogeneity of the superconductors [54]. It was determined from the slope of the $\ln E$ versus $\ln J$ graph and plotted as a function of x (wt.%) as shown in the inset of Fig. 5b. It can be observed that the values of n exhibited an increase from 3.888 for the pure sample to 6.927 for the sample with $x = 0.04$ wt.%, and then decreased to 3.15 for the sample with a higher concentration. This indicates that the sample with $x = 0.04$ wt.% showed the highest value for n , suggesting greater homogeneity. In addition, n is related to the pinning energy through the following relation [55].

$$n \sim \frac{U_0}{K_B T}. \quad (6)$$

The calculated values of U_0 are presented in Fig. 5b as a function of x (wt.%) for all composite samples. It's evident that U_0 values increased as x increased up to $x = 0.04$ wt.%, confirming the positive impact of the nano-(BSF) addition on the superconducting properties of (Bi, Pb)-2223 phase at that doping level. Conversely, for $x > 0.04$ wt.% U_0 decreased, suggesting that high-level doping degraded (Bi, Pb)-2223 properties for the reasons discussed earlier.

3.3.3 Fluctuation-induced conductivity

The fluctuation-induced conductivity, also known as excess conductivity ($\Delta\sigma$), which appears above T_c , is considered one of the most important for understanding the conduction mechanism of HTSC materials and obtaining data on microscopic and superconducting parameters through various models, such as the (A-L) [56], Lawrence-Doniach (L-D) [57], and Maki-Thompson (M-T) [58]. In this study, we used the (A-L)-model to determine the fluctuation-induced conductivity, which can be defined by the following equation:

$$\Delta\sigma = \sigma_m(T) - \sigma_n(T) = \frac{1}{\rho_m(T)} - \frac{1}{\rho_n(T)}, \quad (7)$$

where $\rho_m(T)$ represents the measured electrical resistivity, and $\rho_n(T)$ represents the normal-state resistivity of the composite samples, as listed in Table 3. These values were calculated from the fitting of resistivity measurements as described previously in [4].

Aslamazov and Larkin utilized a microscopic approach within the mean-field region to determine the excess conductivity $\Delta\sigma$. This calculation employs the following relation:

$$\frac{\Delta\sigma}{\sigma_{room}} = A t^\alpha. \quad (8)$$

Herein, t represents the reduced temperature [$t = (T - T_c)/T_c$]. The exponent α differentiates between fluctuation regions, it equals -0.33 for critical fluctuations (Cr), -0.5 for 3-dimension fluctuations (3D), -1.0 for 2-dimension (2D) fluctuations, -1.5 for 1-dimension (1D) fluctuations, and -3.0 for short-wave (SW) fluctuations. A is the temperature-independent amplitude, expressed as in the following Eq. (9):

$$\begin{aligned} A &= \frac{e^2}{32\hbar\xi_c(0)\sigma_{room}} \text{ For (3D),} \\ A &= \frac{e^2}{16\hbar d\sigma_{room}} \text{ For (2D) and} \\ A &= \frac{e^2\xi(0)}{32\hbar s\sigma_{room}} \text{ For (1D).} \end{aligned} \quad (9)$$

where $\xi_c(0)$ is the zero-temperature coherence length along the c -axis, d is the effective layer thickness of the 2D fluctuation and s is the wire cross-sectional area of the 1D fluctuation.

The physical microscopic parameters determined from fluctuation-induced conductivity analysis are greatly influenced by the dimensionality of the fluctuations. Lawrence and Doniach modified the (A-L)-model for polycrystalline and layered superconductors [16, 59]. In cuprate

superconductors, superconductivity happens principally in 2D CuO₂ planes. In this model the excess conductivity $\Delta\sigma$ is given by:

$$\Delta\sigma = \frac{e^2}{16\hbar d} (1 + Jt^{-1})^{-0.5} t^{-1}, \tag{10}$$

where $J = (2\xi_c(0)/d)^2$ is Josephson inter-layer coupling strength. For weak coupling ($J \ll 1$), the L–D relation cut down to the 2D fluctuations case in the AL model ($\alpha = -1$ in Eq. (8)), and for the strong coupling ($J \gg 1$) cutbacks to the 3D condition ($\alpha = -0.5$ in Eq. (8)). The intersection temperature between 2 and 3D conduction regimes expresses by.

$$T^{3D-2D} = T_c \left[1 + \left(\frac{2\xi_c(0)}{d} \right)^2 \right]. \tag{11}$$

The excess conductivity, $\Delta\sigma$, was calculated using Eq. (7) for all nano-(BSF)_x/(Bi, Pb)-2223 composite samples. To analyze the fluctuation-induced conductivity, the $\text{Ln}(\Delta\sigma/\sigma_{\text{room}})$ vs $\text{Ln}(t)$ curves were plotted for all samples, and samples with $x = 0.00, 0.04, 0.05$ and 0.20 wt.% are displayed in Fig. 6 as examples. Each plot revealed the presence of three

distinct regions: the Cr, mean-field (MF), and SW regions. The MF region of each composite sample subtends into the 2D and 3D fluctuation regions. The different regions were fitted linearly, and the α values as well as the intersection temperatures $T^{\text{Cr}-3D}$, T^{3D-2D} , and T^{2D-SW} were determined and displayed on the graph of samples in Fig. 6.

The short-wave region, which exhibits a fluctuation-induced conductivity exponent $\alpha \approx -3$, occurs at temperatures significantly higher than T_c . This indicates that in this region, the Ginzburg–Landau (GL) theory is violated, and SW fluctuations play the predominant role. This phenomenon primarily occurs when the order parameter's characteristic wavelength and coherence length are comparable [16]. These behaviors are associated with variations in the carrier density or the band structure and the shape of the Fermi surface [14, 60, 61]. As the temperature decreases, a transition from the SW region to the 2D fluctuation region occurs at the temperature T^{2D-SW} . As illustrated in Fig. 6, the 2D fluctuation-induced conductivity exponent α is ≈ -1 . In this region, charge carriers predominantly move along the CuO₂ planes, and conductivity primarily arises from charge carriers restricted within the CuO₂ planes [16, 62]. When the temperature is lowered to nearing T_c , the 3D fluctuation

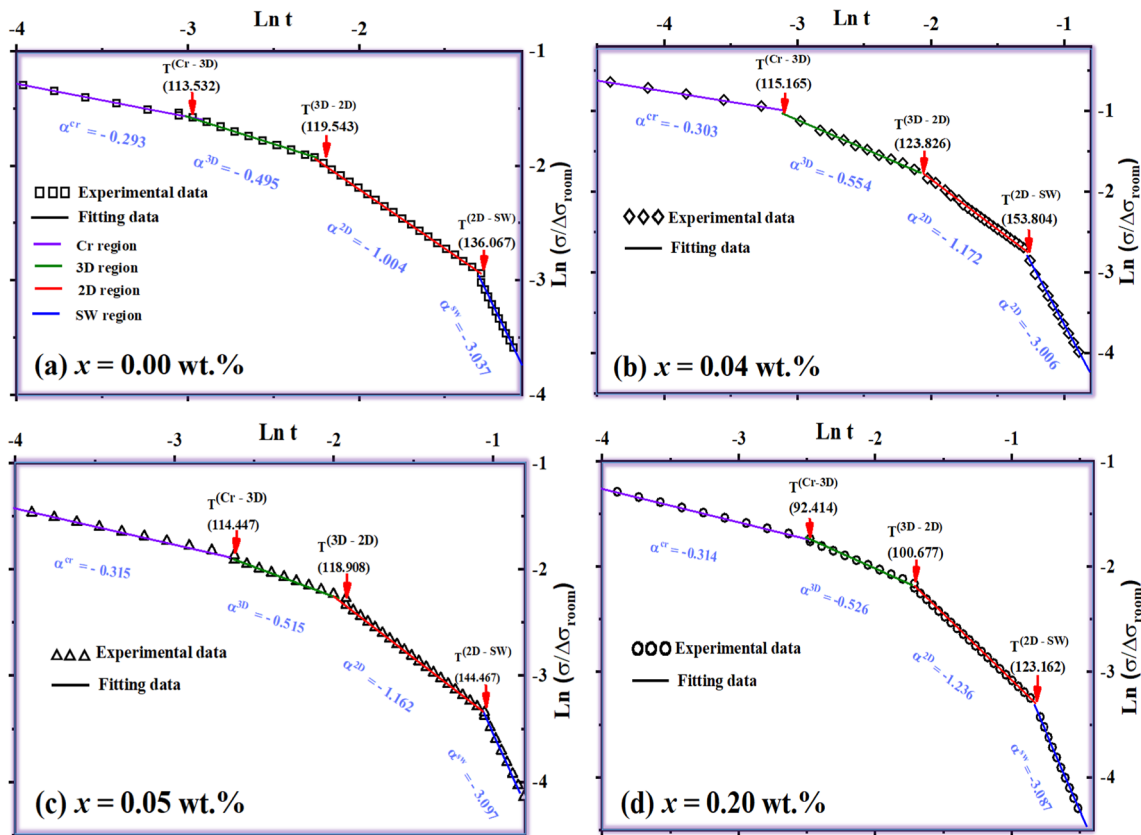


Fig. 6 Variation of the normalized excess conductivity $\text{ln}(\Delta\sigma/\sigma_{\text{room}})$ versus $\text{ln}(t)$ plot for nano-(BSF)_x/(Bi, Pb)-2223 samples with $x = 0.00, 0.04, 0.05,$ and 0.20 wt. %

region begins at T^{3D-2D} , and the conductivity exponent α decreases to ≈ -0.5 as shown in Fig. 6. In this region, charge carriers traverse the barrier layers to access the conducting CuO₂ layers. They move between the planes and are influenced more significantly by thermal fluctuations compared to the 2D region. This suggests that the charge carriers tend to move with greater freedom throughout the entire sample before the formation of Cooper pairs. Thus, the intersection between the 2D and 3D aspects can be characterized as aligning with the high anisotropy of the high-temperature superconducting HTSC materials [14, 17, 63, 64]. It is noted that, the values of 3D-2D cross-over temperature T^{3D-2D} are decreased with increasing the nano-(BSF). This suggests that T^{3D-2D} is a sensitive parameter for the electronic structure in the normal state and can be notably affected by the concentration of nano-(BSF) [7]. As the temperature decreases further, a transition occurs from three-dimensional fluctuations to critical fluctuations at Ginzburg temperature T_G , with critical exponent values ≈ -0.3 as shown in Fig. 6. These values are in line with predictions from the 3D-xy universality class, as described by the representative of Hohenberg and Halperin model [65]. The model is founded on the coupling of a 2D superconducting order parameter with a symmetry-breaking field (SBF). In the critical region below T_G , fluctuations in the order parameter reach a magnitude comparable to the order parameter itself [66], rendering the GL theory unsuitable [7].

The $\xi_c(0)$, d , and J were calculated by determining the values of T^{2D-3D} , through the analyses of the fluctuation-induced conductivity for each sample and using the LD model Eq. (11), and listed in Table 4. It is noted that all inter-layer coupling strength values $J < 1$, which means the coupling between the CuO₂ planes is weak, which is a common feature of oxide superconductors [67]. The $\xi_c(0)$ and the d decrease as the nano-(BSF) concentration increases up to $x = 0.04$. This illustrates the enhancement in the connectivity between the grains as observed in SEM analysis and the hole concentration in the conducting CuO₂ planes [68]. Then they increase again with a

further increase in nano-(BSF). The shortest coherence length and the lowest J values are estimated for the composite sample is generally a feature of the HTSC materials and is due to the energy bands overlapping [69].

In addition, the thermodynamic critical field $B_c(0)$ is calculated using the Ginzburg number N_G according to the following equation[70].

$$N_G = \left| \frac{T_G - T_c}{T_c} \right| = \frac{1}{2} \left[\frac{K_B}{B_c^2(0)\Gamma^2\xi_c^3(0)} \right]^2, \tag{12}$$

where k_B is Boltzmann’s constant, and Γ is the anisotropy parameter equal to 35 for the (Bi, Pb)-2223 superconducting phase [7]. Furthermore, the Ginzburg–Landau equations allow the derivation of several significant superconducting parameters, including the $B_{c1}(0)$, $B_{c2}(0)$, $\lambda_{pd}(0)$, and $J_c(0)$.

$$B_c(0) = \frac{\Phi_0}{2\sqrt{2}\pi\lambda_{pd}\xi_c(0)}, \tag{13}$$

$$B_{c1}(0) = \frac{B_c(0)}{\kappa\sqrt{2}\pi} \ln \kappa, \tag{14}$$

$$B_{c2}(0) = \sqrt{2}\kappa B_c(0) \text{ and} \tag{15}$$

$$J_c(0) = \frac{4kB_{c1}(0)}{3\sqrt{3}\pi\lambda_{pd}\ln \kappa}. \tag{16}$$

where $\Phi_0 = h/2e$ is the flux-quantum number and $\kappa = \lambda_{pd}/\xi_c(0)$ is the Ginzburg–Landau parameter.

Furthermore, the v_F and E_F of charge carriers are calculated from Eqs. (17) and (18) and summarized in Table 4:

$$v_F = \frac{3.5\pi K_B T_c \xi_c(0)}{2\hbar} \text{ and} \tag{17}$$

Table 4 Variation of the estimated superconducting parameters of nano-(BSF)_x/(Bi, Pb)-2223 composite samples with $0.00 \leq x \leq 0.20$ from excess conductivity analyses

x (wt.%)	$\xi_c(0)$ (Å)	d (Å)	J	λ_{pd} (Å)	K	$B_c(0)$ (T)	$B_{c1}(0)$ (T)	$B_{c2}(0)$ (T)	$J_c(0) \times 10^3$ (A/cm ²)	$V_F \times 10^5$ (m/s)	E_F (eV)
0.00	32.987	208.753	0.100	717.907	21.763	0.983	0.098	30.245	0.745	2.560	1.863
0.01	27.053	203.474	0.071	569.457	21.050	1.511	0.155	44.969	1.444	2.112	1.269
0.02	26.237	187.713	0.078	563.614	21.482	1.574	0.159	47.809	1.520	2.071	1.219
0.03	20.447	148.855	0.075	495.070	24.213	2.299	0.214	78.720	2.528	1.632	0.757
0.04	17.642	134.308	0.069	432.002	24.487	3.053	0.282	105.740	3.847	1.428	0.580
0.05	20.043	173.892	0.053	586.828	29.278	1.979	0.161	81.922	1.835	1.552	0.685
0.10	35.230	202.321	0.121	649.850	18.446	1.016	0.114	26.516	0.851	2.554	1.854
0.20	38.331	267.630	0.082	842.535	21.981	0.721	0.072	22.399	0.465	2.373	1.601

$$E_F = \frac{m^* v_F^2}{2}. \quad (18)$$

where m^* is the electron effective mass at fermi level equal $10m_0$ [71].

From Table 4, it is clear that the values of the parameters $B_c(0)$, $B_{c1}(0)$, $B_{c2}(0)$, and $J_c(0)$ increase as the concentration of nano-(BSF) increases up to $x=0.04$ wt.%, then decrease for $x>0.04$ wt.%. Conversely, λ_{pd} , v_F and E_F exhibit the opposite trend, decreasing with an increase in nano-(BSF) concentration up to $x=0.04$ wt.% and then increasing with further increase in nanoparticle concentrations. The increase of parameters $B_c(0)$, $B_{c1}(0)$, $B_{c2}(0)$, and $J_c(0)$, and the decreases of the λ_{pd} , v_F and E_F with the small amount of the nanoparticle concentration up to $x=0.04$ wt.% reflects an enhancement in the nano-(BSF)_x/(Bi, Pb)-2223 composite samples properties. This enhancement can be attributed to an increase in inter-grain connections and a reduction in the number of weak links, as previously observed in SEM analysis, resulting in the reduction in the vortices motion, which in turn prevents the flux creep by improving the flux pinning ability inside the composite resulting of hard

magnetic nano-(BSF) addition, which act as strong pinning centers. These results are consistent with the findings reported by Aftabi et al. [16] when they investigated the fluctuation-induced conductivity of the (Bi, Pb)-2223 phase with the addition of ZnO nanoparticles. Conversely, a further increase in nanoparticle concentration diminishes the properties of the nano-(BSF)_x/(Bi, Pb)-2223 composite samples.

3.3.4 Magnetoresistance measurements analysis

The temperature dependent resistivity of nano-(BSF)_x/(Bi, Pb)-2223 composites were measured at different applied magnetic fields and depicted in Fig. 7.

As seen in Fig. 7 all samples exhibit metallic-like behavior in the normal state above the onset superconducting transition temperature T_c^{on} , followed by broadening tail, accompanied by a shift in the T_0 with increasing applied magnetic field. This behavior can be explained as follows: there are two regions where the magnetic field can affect the resistivity curve. The first region takes place in the normal state ($T>T_c$), where the normal-state resistivity changes very slightly as the applied magnetic field

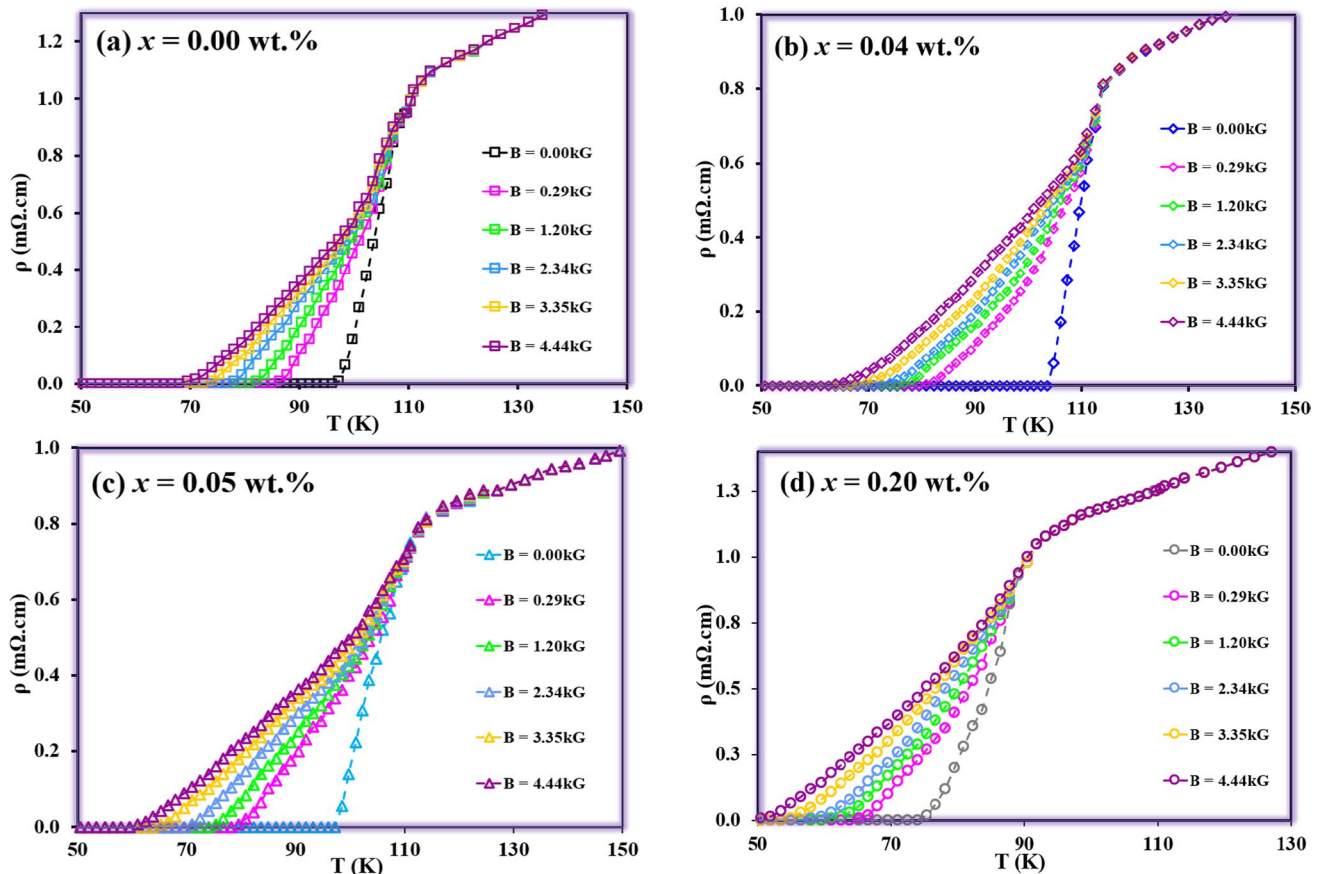


Fig. 7 Variations of resistivity dependence on temperature at different applied DC magnetic fields for nano-(BSF)_x/(Bi, Pb)-2223 composite with $x=0.00, 0.04, 0.05,$ and 0.20 wt.%

increases, primarily as a result of defects and inhomogeneities in the samples [72, 73]. The second region is the mixed-state region, which encompasses both the pairing transition and the tail part; In the pairing transition part, associated with the transition from isolated grains to the superconducting state T_c^{on} , there may be some alteration when magnetic fields are applied. This alteration suggests the presence of significant intra-grain energy that constrains vortex motion [74]. Here, it turns out that the broadening tail part of the resistivity curve is extremely sensitive to the applied magnetic field, even at low magnetic field strengths. This sensitivity arises from the penetration of flux into the intergranular regions, which are characterized by weak coupling between grains. Consequently, the tail part shifts to lower temperatures with an increase in the applied magnetic field [75, 76].

The TAFC model of Anderson and Kim [77], used to describe the broadening tail part, results from the thermally assisted motion of magnetic flux [75, 78, 79]. To gain a deeper understanding of the impact of additive

nanoparticles on the flux pinning energy of nano-(BSF)_x/(Bi, Pb)-2223 samples, the Arrhenius equation was employed [39, 80]:

$$\rho(B, T) = \rho_0 \text{Exp} \left[-\frac{U(B, T)}{K_B T} \right]. \tag{19}$$

Here, $U(B, T)$ represents the flux pinning energy, which depends on both temperature and magnetic field, while ρ_0 is the pre-exponential factor independent of applied magnetic fields and orientation and K_B is Boltzmann's constant.

The field dependent $U(B)$ was determined from the low resistivity part of the broadening by calculating the slopes of linear portions in $\ln(\rho/\rho_0)$ vs $\ln(1/T)$ curves. Figure 8 displays the $\ln(\rho/\rho_0)$ vs $\ln(1/T)$ curves for some selected samples. The obtained $U(B)$ values were fitted to a power law relation according to Eq. (20) for all samples and illustrated in Fig. 9a.

$$U(B) \sim B^{-\beta}. \tag{20}$$

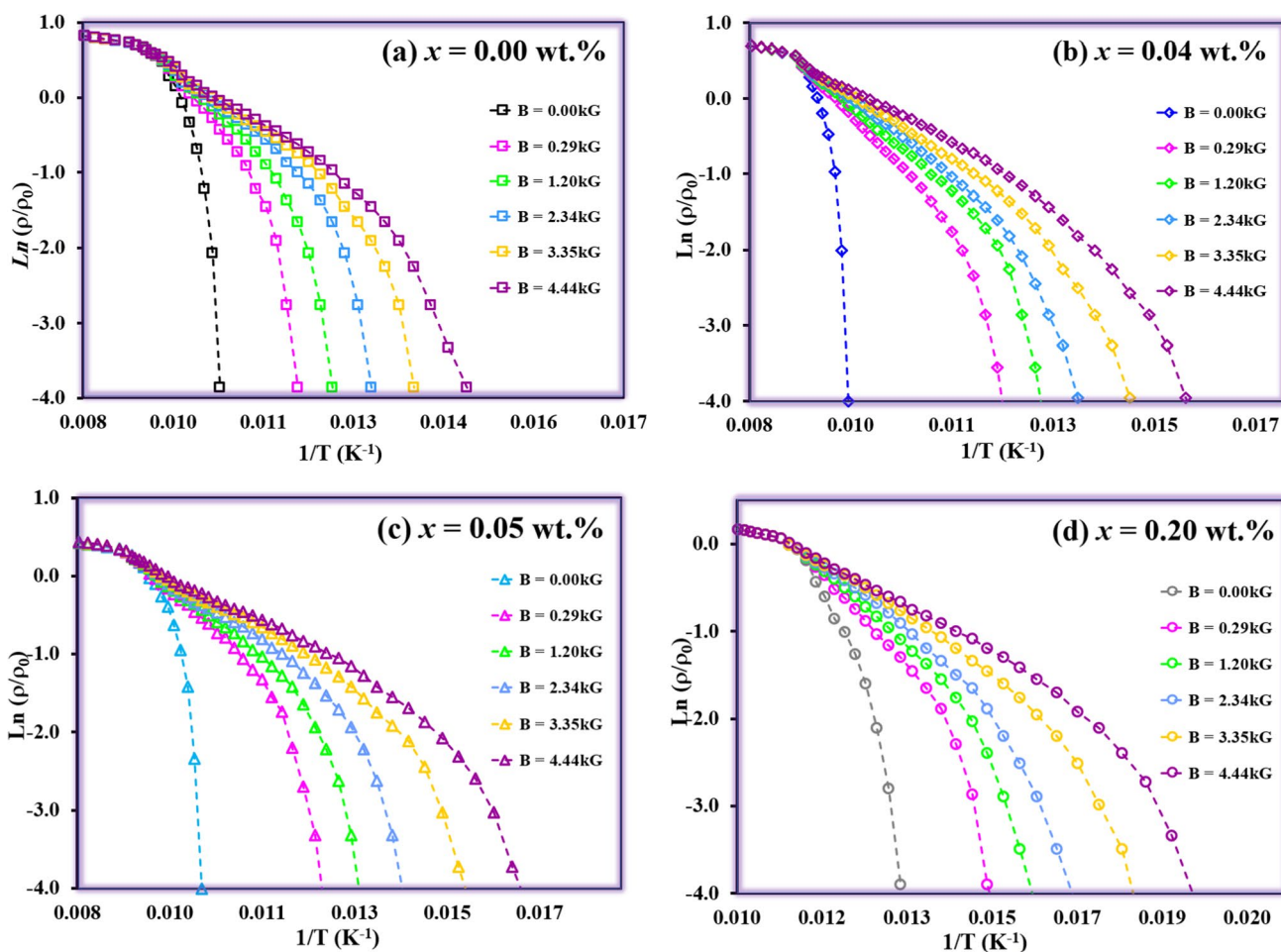


Fig. 8 Variations of $\ln(\rho/\rho_0)$ vs $\ln(1/T)$ of the nano-(BSF)_x/(Bi, Pb)-2223 composite samples with $x=0.00, 0.04, 0.05,$ and 0.20 wt.% at different applied DC magnetic fields

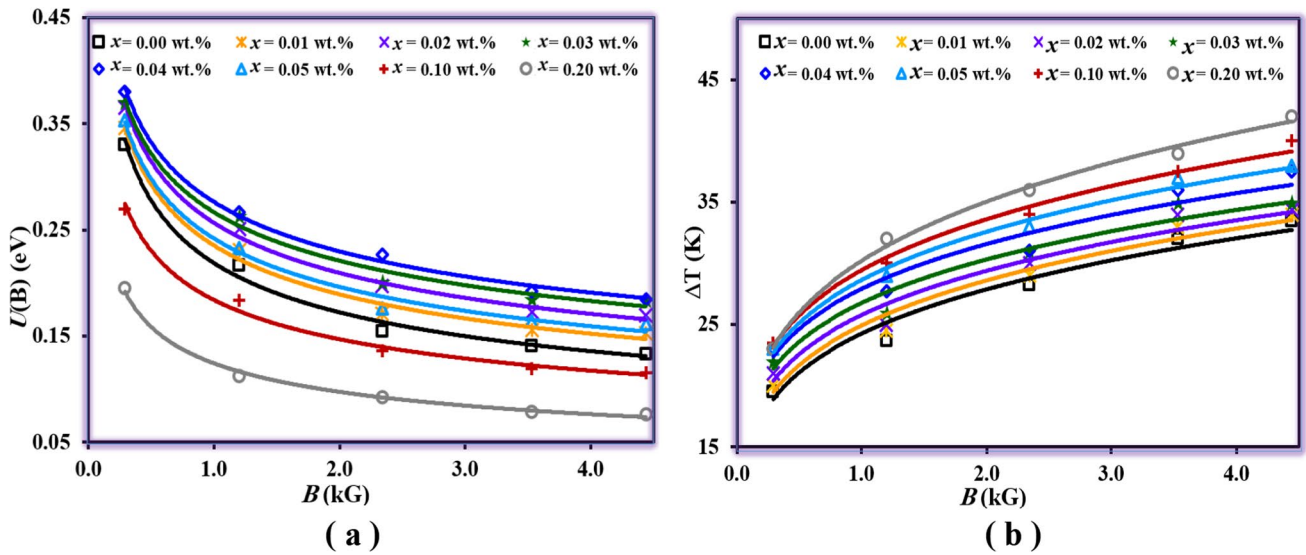


Fig. 9 **a** Variation of flux pinning energy $U(B)$, and **b** superconducting transition temperature width (ΔT) for nano-(BSF) $_x$ (Bi, Pb)-2223 composite samples with $0.00 \leq x \leq 0.20$ at various DC magnetic fields

Here, β represents an exponent that relies on the orientation of the magnetic field relative to the basal plane [81]. As administrated in Fig. 10b the values of β for all samples are obtained in the range of (0.267–0.351), which are in good agreement with other reports [20, 24, 82].

As shown in Fig. 9a, $U(B)$ values for all composite samples rapidly decreased with increasing applied magnetic field up to 2.89kG. Afterward, the rate of decrease slowed, and the values essentially plateaued as the applied field strength increased to 4.44 kG. It is also noteworthy that the flux pinning energies of the composite samples significantly increase with an increase of nanoparticle

concentration up to $x = 0.04$ wt.%. However, they start to decrease when $x > 0.04$ wt.%. This indicates that the flux pinning energies have been improved until they reach an optimum nanoparticle concentration at $x = 0.04$. This improvement can be attributed to the fact that a concentration of 0.04 wt.% of nano-(BSF) leads to an increase in the number of pinning centers, thereby enhancing the flux pinning mechanism. This, in turn, results in an improvement in energy barriers required for flux pinning, preventing the penetration of the applied magnetic field into the sample. This observation is consistent with the interpretation of an increase in intergranular coupling and a reduction in

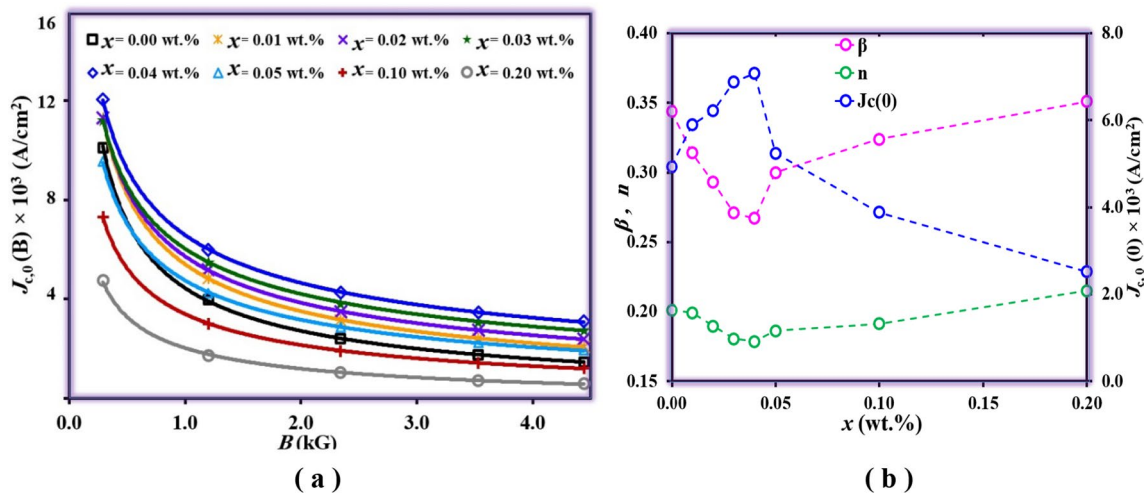


Fig. 10 **a** Variation of $J_{c,0}(0)$ for nano-(BSF) $_x$ (Bi, Pb)-2223 composites with $0.00 \leq x \leq 0.20$ at various magnetic fields and **b** variation of parameters β , n and $J_{c,0}(0)$ versus x (wt.%)

the number of weak links. Consequently, vortices cannot easily exhibit creep behavior due to the relatively high flux pinning energy values, resulting from the reduction in weak links in the sample with $x=0.04$ wt.% in comparison to the other samples. These results align with findings reported by Dogruer et al. [82] when they investigated the addition of Mn to the (Bi, Pb)-2223 phase. Similarly, Barakat et al. [24] reported similar results in their study of the magneto-resistivity of the (Bi, Pb)-2223 phase after adding BaSnO₃ nanoparticles.

Furthermore, the dependence transition width ΔT on the magnetic field for the composite samples were calculated, and their values were fitted according to the power-law by using Eq. (21) [83] and illustrated in Fig. 9b.

$$\Delta T \sim B^n, \quad (21)$$

where n is a constant, Fig. 10b shows that the values of n fall within the range of 0.179 – 0.215, consistent with those obtained for the (Bi, Pb)-2223 phase [20, 82].

As shown in Fig. 9b the ΔT of the composite samples increases with an increase in applied magnetic field strength and the concentration of nano-(BSF) concentration. This increase in ΔT with increasing magnetic fields can be explained as follows: during the cooling process, a greater number of grains with random orientations become frozen and cluster in various positions, acting as defects in the samples. consequently, this leads to weaker vortex pinning, resulting in an increase in the sample resistance due to the increase in the scattering rate and reducing the mean free path of the charge carriers [84]. Furthermore, the increase in ΔT with a higher concentration of nano-(BSF) can be attributed to either the reduction in the volume fraction of the (Bi, Pb)-2223 phase, as discussed in the previous XRD analysis, or the decreased inter-grain connectivity due to the observed large agglomerations and aggregations of nanoparticles between the superconducting grains in the SEM analysis [4].

On the other hand, the flux pinning energy $U(B, T)$ can be evaluated based on the TAFC model and AH theory [85] with the aid of Eq. (22);

$$\frac{\rho}{\rho_n} = \left[I_0 \left(\frac{\gamma(B, T)}{2} \right) \right]^{-2}. \quad (22)$$

Here, ρ_n represents the average normal resistivity, I_0 denotes the modified Bessel function, and $\gamma(B, T)$ is the normalized barrier height defined as $\gamma(B, T) = U(B, T)/K_B T$ [86]. The expression for $U(B, T)$ can be written according to TAFC model as [87, 88]:

$$U(B, T) \sim \Delta T B^{-\eta}, \text{ where } \eta = \beta + n. \quad (23)$$

The differentiation between thermal and magnetic field influences on the normalized barrier height can be reframed from a physical standpoint using the AH theory in the following manner [89]:

$$\gamma(B, T) = C(B)(1 - t)^q. \quad (24)$$

Here, $t = T/T_c$ represents the reduced temperature, $q = \beta/n$, and $C(B)$ is a parameter reliant on the magnetic field and is employed to compute the critical current density at 0 K, as shown in Eq. (25) [89].

$$J_{c,0}(B) = \frac{C(B)eK_B T_c}{\hbar d^2}. \quad (25)$$

Here, d represents the average grain size, which was determined from SEM analysis as described previously in [4].

According to the AH model, the $J_{c,0}(B)$ was determined for the samples at different applied magnetic fields using Eq. (25) and illustrated in Fig. 10 (a). the $J_{c,0}(B)$ values were fitted according to a power-law relation $J_{c,0}(B) \sim B^{-m}$ to obtain the field-independent critical current density values $J_{c,0}(0)$, and displayed versus x (wt.%) in Fig. 10b.

It is evident from Fig. 10a that all curves have a behavior qualitatively similar. The $J_{c,0}(B)$ values show a decrease as the magnetic field increases. This behavior might be explained by the sensitivity of single junctions between superconducting grains to the magnetic field, resulting in a demonstrated drop in $J_{c,0}(B)$ at grain boundaries when the field is increased [21, 90]. Additionally, it is noted in Fig. 10b that the $J_{c,0}(0)$ values increased as the concentration of nano-(BSF) increased until $x=0.04$ wt.%. which means an enhancement in $J_{c,0}(0)$, this enhancement could be attributed to the positive impact of adding nano-(BSF), which improves the inter-granular characteristics of the (Bi, Pb)-2223 phase. Comparable findings were reported by Abou-Aly et al. [20] in their study of the magnetoresistance of Bi_{1.8}Pb_{0.4}Sr₂Ca_{2.1}Cu_{3-x}Ru_xO_{10+δ} and by Govea et al. [21] when investigating the intergranular pinning energy of the (Bi, Pb)-2223 phase during uniaxial compaction. Conversely, the decrease in $J_{c,0}(0)$ for $x > 0.04$ wt.% could be attributed to an increase in grain boundary resistance or the presence of non-superconducting impurities as discussed above.

Finally, Fig. 11 displays the variation of measured J_c (77) and the calculated $J_c(0)$ obtained from fluctuation conductivity and magnetoresistance $J_{c,0}(0)$. The critical current density values of the composite samples consistently follow the same trend with increasing nanoparticle concentration. It's worth mentioning that adding ferrite nanoparticles up to $x=0.04$ wt.% positively enhances the J_c of the (Bi, Pb)-2223 superconducting phase.

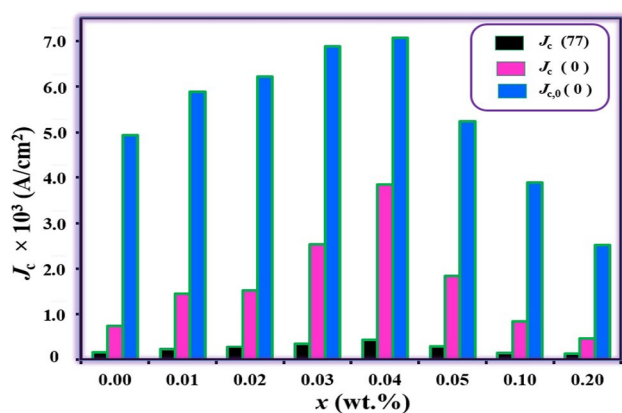


Fig. 11 Variation of $J_c(77)$, $J_c(0)$ and $J_{c,0}(0)$ vs x (wt.%) for the nano-(BSF) $_x$ (Bi, Pb)-2223 composite samples with $(0.00 \leq x \leq 0.20)$

4 Conclusion

In conclusion, this study investigated the impact of hard ferrite nano-(BSF) on the properties of the (Bi, Pb)-2223 superconducting phase over a range of $(0.00 \leq x \leq 0.20)$. The composite samples were examined using EDX, which revealed the presence of all composite elements. It was observed that the nano-(BSF) did not enter the crystalline phase structure. In addition, the results confirmed that the samples were well-homogenized. XPS has been performed to determine their elemental composition and oxidation states. The XPS analysis confirmed that the superconductivity of (Bi, Pb)-2223 is influenced by electron transfer between Bi and Cu ions, as well as variations in oxygen content due to the addition of nano-(BSF). Upon the introduction of nano-(BSF), the hole-carrier concentrations (P) in the composite samples exhibited an increase, rising from 0.138 in the pure sample to 0.160 for samples with $x=0.04$ wt.%, and decreasing for $x > 0.04$ wt.%. The thermoelectric power analysis confirmed that the predominant charge carrier transport mechanism in the CuO_2 planes of the composite samples is through holes. The J_c was measured at 77 K and showed an increase from 151.090 A/cm² for the pure samples to 441.200 A/cm² for the sample with $x=0.04$ wt.%. The analysis of fluctuation-induced conductivity, based on the (A–L)-model, revealed noteworthy changes. Specifically, parameters such as the $\xi_c(0)$, d , $\lambda_{pd}(0)$, v_F and E_F , improved as the concentration of nano-(BSF) increased up to $x=0.04$. Additionally, the critical parameters; $B_{c1}(0)$, $B_{c2}(0)$, and $J_c(0)$, improved by the nano-(BSF) concentration increased up to $x=0.04$, but demonstrated a decrease for $x > 0.04$ wt.%. The magnetoresistance measurements were conducted within the range of (0.29 to 4.44 kG) for the composite samples. These measurements were analyzed using both the TAFC and the AH models. As a result, the flux pinning energy was enhanced, leading to an improvement in the flux pinning mechanism

achieved by adding nano-(BSF) up to $x=0.04$ wt.%. The magnetoresistance results complement the findings from the fluctuation-induced conductivity analysis, indicating that the flux pinning mechanism in the (Bi, Pb)-2223 superconducting phase was enhanced by adding small amounts of nano-(BSF) up to $x=0.04$ wt.%, representing the optimum doping level.

Acknowledgements This study was conducted at the Superconductivity and Metallic Glass Laboratory within the physics department of the Faculty of Science at Alexandria University in Alexandria, Egypt. It was carried out in partnership with the Material Sciences Lab at the Faculty of Science in Beirut Arab University, Lebanon.

Author contribution M. Matar: Investigation, Analysis, Review, and Editing. I. E. Mohamed: Data Collection, Investigation, Analysis, Original Draft Writing. A. I. Abou-Aly: Supervision. R. Awad: Review and Editing. M. Anas: Editing and Proofreading. M.S. Hassan: Investigation, Review, and Editing. All authors read and approved the final manuscript.

Funding Open access funding provided by The Science, Technology & Innovation Funding Authority (STDF) in cooperation with The Egyptian Knowledge Bank (EKB).

Data availability The data that support the findings of this study are available from the corresponding author upon reasonable request.

Declarations

Conflict of interest The authors declare that they have no conflict of interest.

Open Access This article is licensed under a Creative Commons Attribution 4.0 International License, which permits use, sharing, adaptation, distribution and reproduction in any medium or format, as long as you give appropriate credit to the original author(s) and the source, provide a link to the Creative Commons licence, and indicate if changes were made. The images or other third party material in this article are included in the article's Creative Commons licence, unless indicated otherwise in a credit line to the material. If material is not included in the article's Creative Commons licence and your intended use is not permitted by statutory regulation or exceeds the permitted use, you will need to obtain permission directly from the copyright holder. To view a copy of this licence, visit <http://creativecommons.org/licenses/by/4.0/>.

References

1. B. Özkurt, J. Mater. Sci. Mater. Electron. (2014). <https://doi.org/10.1007/s10854-014-2017-9>
2. A.T. Pham, L.H. Vu, D.T. Tran, N.D. Thien, W. Klysubun, T. Miyanaga, N.K. Man, N.T.T. Duong, N.T. Long, P.V. Pham, N.T. Binh, D.H. Tran, Ceram. Int. (2023). <https://doi.org/10.1016/j.ceramint.2022.11.237>
3. S. Vinu, P.M. Sarun, A. Biju, R. Shabna, P. Guruswamy, U. Syamaprasad, Supercond. Sci. Technol. (2008). <https://doi.org/10.1088/0953-2048/21/4/045001>
4. M.S. Hassan, I.E. Mohamed, M. Matar, A.I. Abou-Aly, R. Awad, M. Anas, Appl. Phys. A (2023). <https://doi.org/10.1007/s00339-023-06557-6>

5. M. Anas, M.H. El Makdah, M.H. El Dakdouki, A. Srour, R. Awad, M.S. Hassan, J. Low Temp. Phys. (2023). <https://doi.org/10.1007/s10909-023-02994-y>
6. K. Habanjar, F. El Haj Hassan, R. Awad, Chem. Phys. Lett. (2020). <https://doi.org/10.1016/j.cplett.2020.137880>
7. M. Roumié, W. Abdeen, R. Awad, M. Korek, I. Hassan, R. Mawassi, J. Low Temp. Phys. (2014). <https://doi.org/10.1007/s10909-013-0945-z>
8. W. Zhang, R. Ramesh, J.L. MacManus-Driscoll, H. Wang, MRS Bull. (2015). <https://doi.org/10.1557/mrs.2015.198>
9. K. Zhetpisbaev, Int. J. Electrochem. Sci. (2019). <https://doi.org/10.20964/2019.01.35>
10. N. Ghazanfari, A. Kılıç, Ş. Özcan, H. Sözeri, H. Özkan, A. Gencer, AIP conf, 929 (22 August 2007). <https://doi.org/10.1063/1.2776702>
11. N.R. Mohd Suib, I.P. Abu Bakar, N.B. Ibrahim, R. Abd-Shukor, J. Supercond. Novel Magn. (2019). <https://doi.org/10.1007/s10948-018-4911-5>
12. M.S. Shalaby, M.H. Hamed, N.M. Yousif, H.M. Hashem, Ceram. Int. (2021). <https://doi.org/10.1016/j.ceramint.2021.05.244>
13. L.H. Vu, A.T. Pham, N.D. Thien, N.H. Nam, E. Riviere, Q.N. Pham, N.K. Man, N.T. Binh, N.T.M. Hong, L.V. Cuong, T.L. Nguyen, D.H. Tran, Ceram. Int. (2023). <https://doi.org/10.1016/j.ceramint.2023.06.047>
14. A. Aftabi, M. Mozaffari, A. Moghadam, Mater. Chem. Phys. (2023). <https://doi.org/10.1016/j.matchemphys.2023.128128>
15. T.T. Dung, P.T. An, T.B. Duong, N.K. Man, N. Thi Minh Hien, T. Hai Duc, J. Sci Math. Phys. 37 (2021). <https://doi.org/10.25073/2588-1124/vnumap.4602>
16. A. Aftabi, M. Mozaffari, Sci. Rep. (2021). <https://doi.org/10.1038/s41598-021-83218-9>
17. R. Awad, H.T. Rahal, A.M. Abdel-Gaber, A.I. Abou-Aly, J. Supercond. Novel Magn. (2019). <https://doi.org/10.1007/s10948-019-5035-2>
18. M.K. Ben Salem, Y. Slimani, E. Hannachi, F. Ben Azzouz, M. Ben Salem, Cryogenics (2018). <https://doi.org/10.1016/j.cryogenics.2017.11.005>
19. M. Zouaoui, A. Ghattas, M. Annabi, F.B. Azzouz, M.B. Salem, J. Phys. Conf. Ser. (2009). <https://doi.org/10.1088/1742-6596/150/5/052292>
20. A.I. Abou-Aly, S.A. Mahmoud, R. Awad, M.M.E. Barakat, J. Supercond. Novel Magn. (2010). <https://doi.org/10.1007/s10948-010-0815-8>
21. E. Govea-Alcaide, I. Garcia-Fornaris, P. Mune, R.F. Jardim, Eur. Phys. J. B. (2007). <https://doi.org/10.1140/epjb/e2007-00242-0>
22. T.T.M. Palstra, B. Batlogg, L.F. Schneemeyer, Phys. Rev. Lett. (1988). <https://doi.org/10.1103/PhysRevLett.61.1662>
23. M. Zouaoui, A. Ghattas, M. Annabi, Supercond. Sci. Tech. (2008). <https://doi.org/10.1088/0953-2048/21/12/125005>
24. M.M. Barakat, K. Habanjar, J. Adv. Ceram. (2017). <https://doi.org/10.1007/s40145-017-0222-8>
25. A.I. Abou-Aly, M.M.H. Abdel Gawad, R. Awad, I. G-Eldeen, J. Supercond. Novel Magn. (2011). <https://doi.org/10.1007/s10948-011-1171-z>
26. M. Yassine, N. El Ghouch, A.M. Abdallah, K. Habanjar, R. Awad, J. Alloys Compd. (2022). <https://doi.org/10.1016/j.jallcom.2022.164501>
27. I. Lyuksyutov, D. Naugle, J. Mod. Phys. Lett. B (1999). <https://doi.org/10.1142/S0217984999000622>
28. S.F. Oboudi, J. Supercond. Novel Magn. (2017). <https://doi.org/10.1007/s10948-016-3939-7>
29. M.H. El Makdah, N. El Ghouch, M.H. El-Dakdouki, R. Awad, M. Matar, Ceram. Int. (2023). <https://doi.org/10.1016/j.ceramint.2023.04.070>
30. E.I. Kuznetsova, M.V. Kuznetsov, Y.V. Blinova, T.P. Krinitsina, S.V. Sudareva, E.P. Romanov, D.N. Rakov, Y.N. Belotelova, Phys. Met. Metallogr. (2012). <https://doi.org/10.1134/S0031918X12040072>
31. W. Koichi, Supercond. Sci. Technol. (1998). <https://doi.org/10.1088/0953-2048/11/9/004>
32. H. Yamanaka, H. Enomoto, J.S. Shin, T. Kishimoto, Y. Takano, N. Mori, H.O. HajimeOzaki, Jpn. J. Appl. Phys. (1991). <https://doi.org/10.1143/JJAP.30.645>
33. R. Pattanayak, S. Panigrahi, T. Dash, R. Muduli, D. Behera, Physica B Condens. Matter (2015). <https://doi.org/10.1016/j.physb.2015.06.006>
34. V.V. Atuchin, D.A. Vinnik, T.A. Gavrilova, S.A. Gudkova, L.I. Isaenko, X. Jiang, L.D. Pokrovsky, I.P. Prosvirnin, L.S. Mashkovtseva, Z. Lin, J. Phys. Chem. C (2016). <https://doi.org/10.1021/acs.jpcc.5b12243>
35. A.E. Bocquet, A. Fujimori, T. Mizokawa, T. Saitoh, H. Namatame, S. Suga, N. Kimizuka, Y. Takeda, M. Takano, Phys. Rev. B Condens. Matter (1992). <https://doi.org/10.1103/physrevb.45.1561>
36. B.R. Sekhar, P. Srivastava, N.L. Saini, K.V.R. Rao, S.K. Sharma, K.B. Garg et al., Physica C Supercond. (1993). [https://doi.org/10.1016/0921-4534\(93\)90713-Z](https://doi.org/10.1016/0921-4534(93)90713-Z)
37. G.V.S. Bera, E.P. Amaladass, T.G. Kumary, R. Pandian, A. Mani, Phys. Chem. Chem. Phys. (2021). <https://doi.org/10.1039/D1CP01262B>
38. D.K. Rai, A.K. Sarkar, T.N. Wittberg, B. Kumar, J. Appl. Phys. (1989). <https://doi.org/10.1063/1.344027>
39. A. Aftabi, M. Mozaffari, J. Alloys Compd. (2022). <https://doi.org/10.1016/j.jallcom.2022.164455>
40. O. Bilgili, Y. Selamet, K. Kocabaş, J. Supercond. Novel Magn. (2008). <https://doi.org/10.1007/s10948-008-0374-4>
41. D.H. Tran, T.M. Le, T.H. Do, Q.T. Dinh, N.T.T. Duong, D.T.K. Anh, N.K. Man, D. Pham, W.-N. Kang, Mater. Trans. (2018). <https://doi.org/10.2320/matertrans.MD201715>
42. D.I. Khomskii, F.V. Kusmartsev, *Temperature-Induced Redistribution of Holes and Properties of High Temperature Superconductors* (Springer Netherlands, Dordrecht, 1992), pp. 113–124. https://doi.org/10.1007/978-94-011-2462-1_9
43. P.M. Chaikin, G. Beni, Phys. Rev. B (1976). <https://doi.org/10.1103/PhysRevB.13.647>
44. J.R. Cooper, B. Alavi, L.W. Zhou, W.P. Beyermann, G. Grüner, Phys. Rev. B (1987). <https://doi.org/10.1103/PhysRevB.35.8794>
45. S.D. Obertelli, J.R. Cooper, J.L. Tallon, Phys. Rev. B (1992). <https://doi.org/10.1103/PhysRevB.46.14928>
46. S. Eley, A. Glatz, R. Willa, J. Appl. Phys. (2021). <https://doi.org/10.1063/5.0055611>
47. W.-K. Kwok, U. Welp, A. Glatz, A.E. Koshelev, K.J. Kihlstrom, G.W. Crabtree, Rep. Prog. Phys. (2016). <https://doi.org/10.1088/0034-4885/79/11/116501>
48. M. Dahiya, R. Kumar, D. Kumar, N. Khare, J. Alloys Compd. (2021). <https://doi.org/10.1016/j.jallcom.2021.160840>
49. G.O. Zimmerman, Phys. Today (2007). <https://doi.org/10.1063/1.2743130>
50. M. Nikolo, *Flux Dynamics in High-Temperature Superconductors* (1993), p. 618. <https://doi.org/10.1088/0953-2048/6/8/011>
51. O.V. Kharissova, E.M. Kopnin, V.V. Maltsev, N.I. Leonyuk, L.M. León-Rossano, I.Y. Pinus, B.I. Kharisov, Crit. Rev. Solid State Mater. Sci. (2014). <https://doi.org/10.1080/10408436.2013.836073>
52. V.R. Gómez, I.d.C.d.M.d. Barcelona, U.A.d.B.D.d. Física, *Controlling Vortex Pinning and Dynamics of Nanostructured YBCO Thin Films Grown by Chemical Solution Deposition* (2014). <http://hdl.handle.net/10803/133329>

53. W. Abdeen, S. Marhaba, R. Awad, A.I. Abou Aly, I.H. Ibrahim, M. Matar, J. Adv. Ceram. (2016). <https://doi.org/10.1007/s40145-015-0173-x>
54. R. Mawassi, S. Marhaba, M. Roumié, R. Awad, M. Korek, I. Hassan, J. Supercond. Noval Magn. (2014). <https://doi.org/10.1007/s10948-013-2408-9>
55. N.H. Mohammed, A.I. Abou-Aly, M.M. Barakat, M.S. Hassan, Mod. Phys. Lett. B (2018). <https://doi.org/10.1142/S0217984918501786>
56. L.G. Aslamazov, A.I. Larkin, *Effect of Fluctuations on the Properties of a Superconductor Above the Critical Temperature* (World Scientific, Singapore, 1996). https://doi.org/10.1142/9789814317344_0004
57. W.E. Lawrence, S. Doniach, Proc. of LT (1970)
58. K. Maki, R.S. Thompson, Phys. Rev. B (1989). <https://doi.org/10.1103/PhysRevB.39.2767>
59. Y. Slimani, J. Mater. Sci. Mater. Electron. (2020). <https://doi.org/10.1007/s10854-019-02846-0>
60. M.R. Cimberle, C. Ferdeghini, E. Giannini, D. Marre, M. Putti, A. Siri, F. Federici, A. Varlamov, Phys. Rev. B (1997). <https://doi.org/10.1103/PhysRevB.55.R14745>
61. A.K. Ghosh, A.N. Basu, Phys. Rev. B (1999). <https://doi.org/10.1103/PhysRevB.59.11193>
62. J.Y. Oh, J. Alloys Compd. (2019). <https://doi.org/10.1016/j.jallcom.2019.07.029>
63. A.I. Abou-Aly, R. Awad, I.H. Ibrahim, W. Abdeen, Solid State Commun. (2009). <https://doi.org/10.1016/j.ssc.2008.12.003>
64. A. Sedky, A. Salah, J. Low Temp. Phys. (2020). <https://doi.org/10.1007/s10909-020-02492-5>
65. P.C. Hohenberg, B.I. Halperin, Rev. Mod. Phys. (1977). <https://doi.org/10.1103/RevModPhys.49.435>
66. C.J. Lobb, Phys. Rev. B (1987). <https://doi.org/10.1103/PhysRevB.36.3930>
67. C.P. Poole, H.A. Farach, R.J. Creswick, R. Prozorov, *12—Type II Superconductivity* (Academic Press, Amsterdam, 2007), pp. 337–383. <https://doi.org/10.1016/B978-012088761-3/50034-X>
68. G. Hussain, A. Jabbar, I. Qasim, M. Mumtaz, K. Nadeem, M. Zubair, S.Q. Abbas, A.A. Khurram, J. Appl. Phys. (2014). <https://doi.org/10.1063/1.4895051>
69. K. Habanjar, F. Haj Hassan, R. Awad, Mater. Res. Express (2019). <https://doi.org/10.1088/2053-1591/ab2b07>
70. A. Petrovie, Y. Fasano, R. Lortz, M. Decrouc, M. Potel, R. Chevrel, O. Fischer, Physica C (2007). <https://doi.org/10.1016/j.physc.2007.03.380>
71. I.V. Driessche, A. Buekenhoudt, K. Konstantinov, E. Brueneel, S. Hoste, Appl. Supercond. (1996). [https://doi.org/10.1016/S0964-1807\(96\)00025-7](https://doi.org/10.1016/S0964-1807(96)00025-7)
72. A. Aliabadi, Y.A. Farshchi, M. Akhavan, Phys. C Supercond. Appl. (2009). <https://doi.org/10.1016/j.physc.2009.09.003>
73. H. Chu, J. Li, S. Li, Y. Zhang, N. Wang, J. Wang, Y. Gao, H. Deng, X. Sun, D. Zheng, Sci. China Phys. Mech. Astron. (2010). <https://doi.org/10.1007/s11433-010-4049-3>
74. R. Gross, P. Chaudhari, D. Dimos, A. Gupta, G. Koren, Phys. Rev. Lett. (1990). <https://doi.org/10.1103/PhysRevLett.64.228>
75. M.S. Hassan, A. Khalaf, A. Kamar, R. Awad, M. Matar, Appl. Phys. A (2022). <https://doi.org/10.1007/s00339-022-06170-z>
76. S. Ahmad, N.A. Khan, A.A. Khurram, S. Hussain, J. Supercond. Novel Magn. (2014). <https://doi.org/10.1007/s10948-014-2711-0>
77. P.W. Anderson, Phys. Rev. Lett. (1962). <https://doi.org/10.1103/PhysRevLett.9.309>
78. T.T.M. Palstra, B. Batlogg, R.B. Dover, Phys. Rev. B (1990). <https://doi.org/10.1103/PhysRevB.41.6621>
79. M.H. Pu, Z.S. Cao, Q.Y. Wang, Y. Zhao, Supercond. Sci. Technol. (2006). <https://doi.org/10.1088/0953-2048/19/6/008>
80. Ş Çelik, K. Öztürk, E. Yanmaz, J. Alloys Compd. (2008). <https://doi.org/10.1016/j.jallcom.2007.02.016>
81. B. Özçelik, M. Gürsul, F. Karaçora Nane, J. Mater. Sci. Mater. Electron. 29 (2018). <https://doi.org/10.1007/s10854-018-0041-x>
82. M. Dogruer, Y. Zalaoglu, A. Varilci, J. Supercond. Noval Magn. (2012). <https://doi.org/10.1007/s10948-012-1403-x>
83. V.V. Gridin, T.W. Krause, P.K. Ummat, W.R. Datars, Solid State Commun. (1991). [https://doi.org/10.1016/0038-1098\(91\)90367-5](https://doi.org/10.1016/0038-1098(91)90367-5)
84. A.I. Abou-Aly, M.T. Korayem, N.G. Gomaa, Supercond. Sci. Tech. (1999). <https://doi.org/10.1088/0953-2048/12/3/007>
85. M. Tinkham, Phys. Rev. Lett. (1988). <https://doi.org/10.1103/PhysRevLett.61.1658>
86. H. Khosroabadi, V. Daadmehr, M. Akhavan, Physica C (2003). [https://doi.org/10.1016/S0921-4534\(02\)01876-2](https://doi.org/10.1016/S0921-4534(02)01876-2)
87. L. Zhang, J.Z. Liu, M.D. Lan, P. Klavins, R.N. Shelton, Physica C Supercond. (1994). [https://doi.org/10.1016/0921-4534\(94\)90975-X](https://doi.org/10.1016/0921-4534(94)90975-X)
88. P. Kameli, H. Salamati, I. Abdolhosseini, D. Sohrabi, Physica C Supercond. (2008). <https://doi.org/10.1016/j.physc.2007.10.015>
89. V. Ambegaokar, B.I. Halperin, Phys. Rev. Lett. (1969). <https://doi.org/10.1103/PhysRevLett.22.1364>
90. A.C. Wright, K. Zhang, A. Erbil, Phys. Rev. B (1991). <https://doi.org/10.1103/PhysRevB.44.863>

Publisher's Note Springer Nature remains neutral with regard to jurisdictional claims in published maps and institutional affiliations.